

Calibration of Li-Ion Cathode Materials for Discrete Element Method Simulations

Clemens Lischka* and Hermann Nirschl

The flow behavior of cohesive NMC-622 cathode active material is studied in a Schulze RST-01 ring shear cell and a rotating drum. For both devices, experiments and simulations are done to characterize the dynamic behavior of the material and to calibrate all relevant parameters for a coarse-grained simulation model based on the discrete element method (DEM). The experimental values are directly used to simulate both of the calibration devices to verify a robust simulation model. It is found that for a coarse-graining factor of 200 the characteristic flow mechanics in the experiments and simulations are in overall good agreement. It is further investigated if the aging process of NMC-622 active material has an influence of the macroscopic flow characteristics of the powder. For this, the material was stored in ambient atmosphere for 12 months and investigated afterward by means of ring shear cell measurements and scanning electron microscope imaging. It is found that the aging of NMC-622 leads to changed values for friction coefficients, which can be explained by possible surface reactions of the material in ambient atmosphere. The calibrated DEM model is suitable to be used in further work to provide simulative insides into the production of Li-Ion batteries.

1. Introduction and Motivation

The growing global demand for low-cost electromobility requires further optimization of the battery technology used, as this still represents a major cost factor in the production of an electric car. One focus is not only on increasing the energy density by reducing the addition of so-called conductive additives but also on the solvent-free production of the cathodes to save the energy-intensive drying step during manufacture. Manufacturing processes that do not require solvents are referred to as solvent-free cathode production. A further improvement in energy density can result from a better understanding of the individual process steps, such as mixing and the optimization thereof. To this end, simulation tools are

C. Lischka, H. Nirschl
Institute for Mechanical Process Engineering and Mechanics (MVM)
Karlsruhe Institute of Technology
76131 Karlsruhe, Germany
E-mail: clemens.lischka2@kit.edu

 The ORCID identification number(s) for the author(s) of this article can be found under <https://doi.org/10.1002/ente.202200849>.

© 2022 The Authors. Energy Technology published by Wiley-VCH GmbH. This is an open access article under the terms of the Creative Commons Attribution-NonCommercial License, which permits use, distribution and reproduction in any medium, provided the original work is properly cited and is not used for commercial purposes.

DOI: 10.1002/ente.202200849

increasingly used in research to gain detailed mechanistic insight into each process step. Some authors have used the discrete element method (DEM) to simulate the cathode battery materials.^[1–4] Schreiner and colleagues use DEM to simulate the calendaring process.^[1] They used load-displacement results from experiments to parameterize their DEM model. They found through a sensitivity study that the static friction coefficient of NMC-622 particles had among other parameters significant influence on their simulation results. Giménez and colleagues^[5] used the DEM approach to model the mechanical properties of lithium-ion cathodes with regard to nanoindentation. They found that the elastic behavior of electrodes can be accurately described after the relevant DEM parameters had been calibrated to their experiments.

Mixing, which is at the beginning of the production of a cathode, has been studied by Mayer and colleagues^[6] using computational fluid dynamics (CFD) and DEM methods. They investigated cathode slurry production in a batch process. Asylbekov et al.^[7] studied the shear stress acting on individual carbon black aggregates in a fluid shear flow to model the fracturing of these particles with the DEM method. These DEM simulations have been carried out on the micro-scale since the behavior of only a few individual particles have been simulated. So far in the literature, there has been no description of a simulation model that uses DEM methods to describe the mixing process for Li-Ion materials on the macro-scale. The subject of this work is therefore to contribute to a simulative approach of solvent-free cathode production on the macroscale. A better understanding of the process has the potential to contribute to cost reduction in battery cell manufacturing. In particular, the dry mixing process is considered here using the DEM. In DEM, a number of material parameters such as its friction parameters must be determined for the considered materials to correctly represent their macro-scale flow behavior. Usually, these material parameters are estimated or adjusted based on other experimental data. Since, to the best of the author's knowledge, these material parameters for NMC-622 can not yet been found in the literature, this work aims to contribute to how these relevant DEM parameters can be obtained experimentally and how they can then in turn be used for calibration simulations. Furthermore, the influence of the aging of the NMC-622 on the flow properties is investigated. Some authors report that, under certain storage

conditions, NMC-622 material undergoes a change in surface appearance that may affect the flow properties of the material. Therefore, two different batches of NMC-622 were examined which had been in contact with the ambient air for different periods of time.

2. Experimental Section

2.1. DEM

The DEM was introduced by Cundall in 1979 to simulate the motion of granular materials. The method is based on Newton's equations of motion which are applied to discrete particles. The forces acting on each particle, e.g., the gravitational force or contact forces are balanced.^[8] Equation (1) describes the translational velocity u_i of a particle resulting from the force balance and Equation (2) its rotational velocity ω_i . All forces typically are solved in the 3D vector space but are shown here in a general form.

$$m_i \frac{du_i}{dt} = F_c + F_g \quad (1)$$

$$I_i \frac{d\omega_i}{dt} = F_t \times R_i \quad (2)$$

The contact forces acting on two particles that are in close proximity to each other can be divided into the normal force F_n and the tangential force F_t using Equation (3). These forces are calculated using the coefficients k_n , γ_n , k_t , and γ_t with help of Equation (4)–(14) and the material parameters Y^* , the reduced Young's modulus, G^* the reduced shear modulus, ν , the Poisson's ratio, and e , the coefficient of restitution. The friction coefficients for static and rolling friction are taken into account using additional equations, which can be found elsewhere^[9] for the sake of brevity.

$$F_c = F_n + F_t = (k_n \cdot \delta n_{ij} - \gamma_n \cdot \nu n_{ij}) + (k_t \cdot \delta t_{ij} - \gamma_t \cdot \nu t_{ij}) \quad (3)$$

$$k_n = \frac{4}{3} Y^* \sqrt{R^* \delta_n} \quad (4)$$

$$\gamma_n = -2 \sqrt{\frac{5}{6}} \beta \sqrt{S_n m^*} \geq 0 \quad (5)$$

$$k_t = 8G^* + \sqrt{R^* \delta_n} \quad (6)$$

$$\gamma_t = -2 \sqrt{\frac{5}{6}} \beta \sqrt{S_t m^*} \geq 0 \quad (7)$$

$$S_n = 2Y^* \sqrt{R^* \delta_n} \quad (8)$$

$$S_t = 8G^* \sqrt{R^* \delta_n} \quad (9)$$

$$\beta = \frac{\ln(e)}{\sqrt{\ln^2(e) + \pi^2}} \quad (10)$$

$$\frac{1}{Y^*} = \frac{(1 - \nu_1^2)}{Y_1} + \frac{(1 - \nu_2^2)}{Y_2} \quad (11)$$

$$\frac{1}{G^*} = \frac{2(2 - \nu_1)(1 + \nu_1)}{Y_1} + \frac{2(2 - \nu_2)(1 + \nu_2)}{Y_2} \quad (12)$$

$$\frac{1}{R^*} = \frac{1}{R_1} + \frac{1}{R_2} \quad (13)$$

$$\frac{1}{m^*} = \frac{1}{m_1} + \frac{1}{m_2} \quad (14)$$

Equation (1) allows the modeling of additional, relevant forces such as van-der-Waals interactions or electrostatic forces. As a rule, particles <0.03 mm in diameter behave cohesively,^[10] i.e., attractive forces act between them, which are often modeled in the DEM with help of a cohesion model such as the Simplified-Johnson–Kendall–Roberts model. Equation (15) shows how this force is calculated from the overlapped contact area A (Equation (16)) of the two interacting particles and the cohesion energy density. Values for the cohesion energy density usually have to be determined by comparative experiments for the respective material system.

$$F_{\text{coh}} = kA \quad (15)$$

$$A = \frac{\pi}{4} ((d_{\text{part}} - R_i - R_j) * (d_{\text{part}} + R_i - R_j) * (d_{\text{part}} - R_i + R_j) * (d_{\text{part}} + R_i + R_j)) / d_{\text{part}}^2 \quad (16)$$

The particle velocity and position are solved for numerically by integrating the equations previously described. The computational limitation is the so-called Rayleigh time step (Equation (17)), which forms a stability limit in the calculation.

$$\Delta t_R = \pi R_i \sqrt{\frac{\rho}{G}} (0, 1631\nu + 0, 8766)^{-1} \quad (17)$$

The equations described above are implemented in the open-source DEM software package LIGGGHTS 3.8.0 and were used for all simulations.

2.1.1. Coarse-Graining and Calibration

Since the particle size of NMC-622 particles is in the order of 10 μm ,^[6] very high particle numbers in the order of 10⁹ particles automatically result for the systems under consideration which cannot be calculated with current computer technology on an appropriate time scale. For this reason, the coarse-graining approach has become established in research in which the particle diameter is scaled up by a constant factor^[11–13] (Equation (18)).

$$f_{\text{CG}} = \frac{d_{\text{sim}}}{d_{\text{real}}} \quad (18)$$

In the literature, values of up to 1,000 can be found for the coarse-graining factor.^[14] A coarse-graining factor of 200 was selected for the system under consideration so that the NMC-622 particles of 10 μm are represented by particles of 2 mm diameter in the simulation. This represents the best compromise between computing time and accuracy for planned further simulations on a more application-oriented scale. Since a coarse-graining factor of 200 translates into a reduction of particle count by a factor of 8 \times 10⁶ it can be estimated that the computational cost is reduced by a factor of equal order. In practice, this means a coarse-graining simulation that may take several hours, would

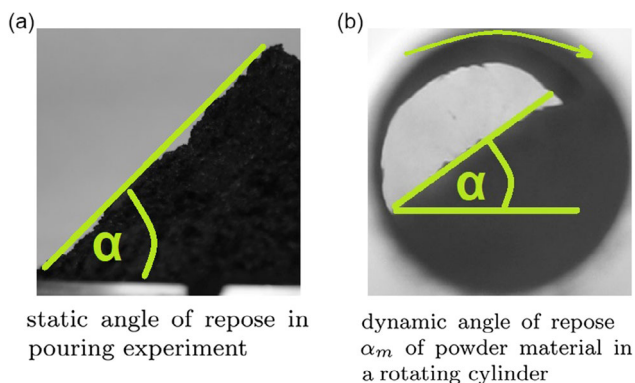


Figure 1. Measurement principles for the a) static and b) dynamic angle of repose.

take years to finish if particle diameters would not be scaled-up. It must be ensured however that the simulated particles behave with sufficient accuracy like the real particle system. To ensure this, so-called calibration experiments are carried out and compared with the behavior of the simulated particle system. There are numerous such calibration experiments in the DEM literature, such as the determination of the bulk density,^[15] the static^[16] (see **Figure 1a**) or dynamic angle of repose^[17] (see **Figure 1b**), measurements in a powder rheometer^[18] or a ring shear cell.^[19–22]

In all of these calibration experiments, the static or dynamic behavior of the examined material is determined. At the same time, the experiment is simulated and results are compared. If there is a sufficiently precise match between the calibration experiment and the simulation, the selected DEM material parameters can be used for further simulation, e.g., here for the dry-mixing process in Li-Ion production. For this work, the ring shear cell and the dynamic angle of repose in a rotating cylinder were chosen as calibration experiments. Numerous authors use the ring shear cell to characterize powders. Often free-flowing materials are used, however, some authors also use ring shear cells for cohesive powders. For example, Legoix

and colleagues^[18] use a ring shear cell to determine the flow of cohesive lactose. The advantage of the ring shear cell is that it provides direct material parameters such as the static and dynamic friction angle via the analysis of the material behavior under shear, which can then be used directly as material parameters in a DEM simulation. For this purpose, the shear cell is reproduced in a computer model on a scale of 1:1 and the shearing at different normal stresses is simulated with the coarse-grained particles of the NMC-622. For the dynamic angle of repose, a rotating cylinder is simulated on a roller bed, in which after a short time a characteristic angle of repose for the material and the considered speed is formed. The advantage of this experiment is its simple setup and the characterization of the dynamic movement, which is a good addition to the static analysis of the material in a ring shear cell.

2.1.2. Ring Shear Cell

An established method for determining the flow properties of powders is the measurement of friction coefficients in shear cells. The Jenike shear cell for example is a device in which the material is sheared translatory. The advantage of a ring shear cell in contrast to the Jenike cell is, that the shear path is infinitely long due to the rotating measuring principle and the measurement is therefore not limited in time. **Figure 2** shows the used Schulze ring shear tester RST-01 with a ring shear cell filled with NMC-622 cathode active material. The annular shear cell consists of a rotating lower part in which the powder to be examined is located, a cover to which the normal stress is applied and two tie rods which, when the lower part rotates, transmit the shear forces through the material to the cover and then to force measuring cells located on the side of the device. With the help of these force-measuring cells, the characteristic course of the shear rate over the rotation time can be recorded. **Figure 3** shows in principle a typical output from the ring shear tester. Measuring the points of incipient flow for different normal stresses (**Figure 3a**) allows the construction of the yield locus. For this, the points of incipient flow and the pre-shear steady state flow are connected to form a line. Under the assumption

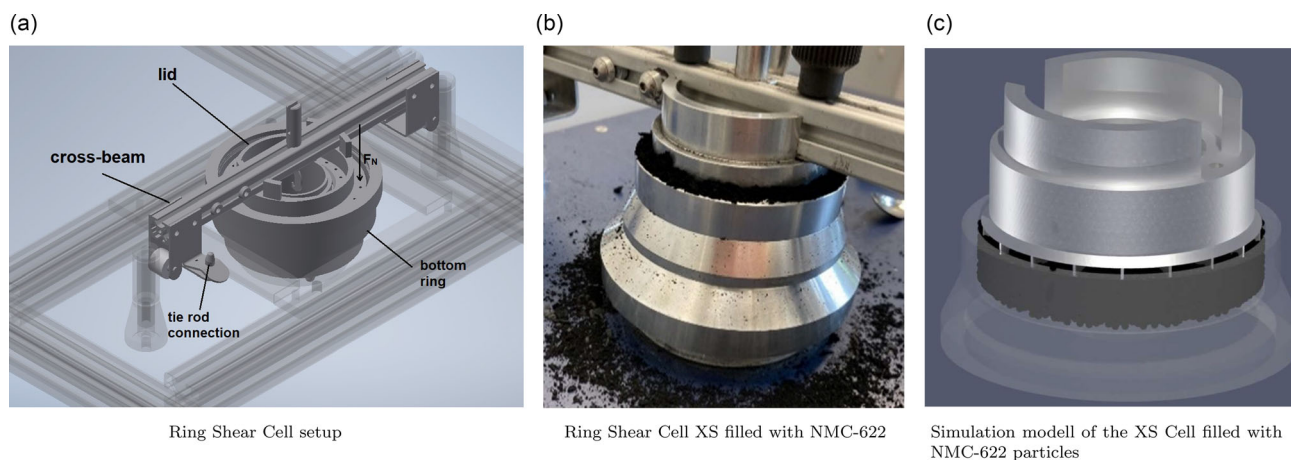


Figure 2. a,b) Experimental and c) simulative setup of the Schulze RST-01 ring shear cell XS cell type filled with NMC-622 material.

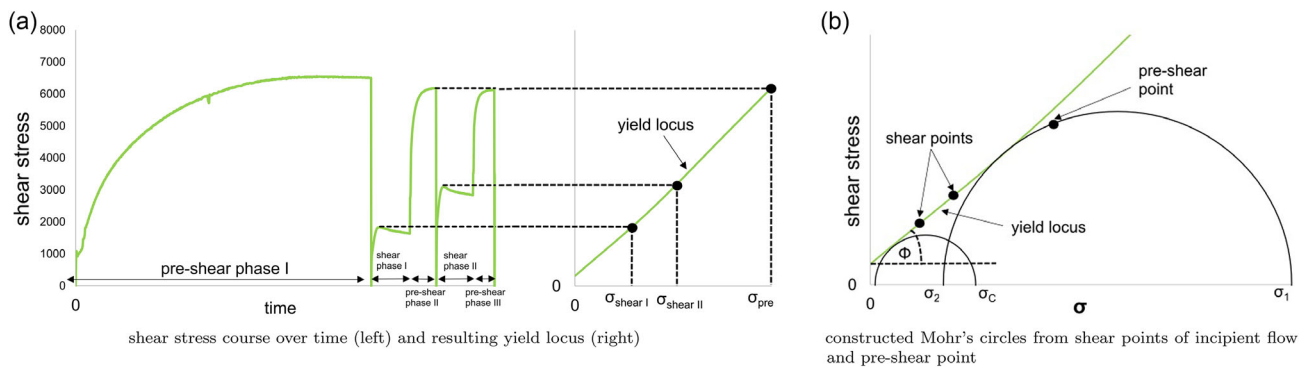


Figure 3. a,b) Principal results from a measurement in ring shear cell test.

that the center of the Mohr circle is on the σ -axis, the pre-shear point is a point on the Mohr circle, and that the Mohr circle touches the constructed yield locus (line) at $\sigma \leq \sigma_{pre}$, the resulting Mohr circle can be constructed. The point of tangency is by definition the end point of the yield locus. The main stresses σ_1 , σ_2 are the intersection points with σ -axis after the Mohr circle is constructed. The unconfined yield strength σ_c is found by constructing a second Mohr circle that fulfills the conditions that its center lies on the σ -axis, the origin ($\sigma = 0$, $\tau = 0$) is a point on the Mohr circle and the circle is also tangent to the yield circle.

The slope of the yield locus characterizes the internal friction angle, from which the friction coefficient can be calculated with Equation (19).

$$\mu = \tan \varphi \quad (19)$$

The process of a measurement consists of filling the measuring cells with the powder to be examined. After filling, the material is smoothed off and the weight of the filled cell is determined. The shear cell cover is then placed on the cell and the cover is connected to the tie rods. At the same time, the desired normal stresses are specified in the program software, which is provided with the Schulze ring shear tester. The actual measurement is made at a constant normal stress for pre-shearing the material. Pre-shearing again between the shear to failure processes is necessary to bring the material back to initial state. After a measurement has been taken, it is usually repeated at least three times by refilling the material accordingly. With the help of the program software, the determined main stresses, the resulting Mohr's stress circles, as well as the friction and cohesion parameters of the material can be calculated and plotted. In addition, the program outputs a detailed time course of the shear rate (like in Figure 3a), which was subsequently used to recreate the experiment in the simulation and to compare the resulting shear curves (see discussion of results later).

2.1.3. Rotating Cylinder

An established method to characterize the movement of powdery bulk solids is the measurement of the dynamic angle of repose in a rotating drum. The bulk material to be analyzed is placed in a

cylinder whose side walls are transparent. Values smaller or equal to 50% are usually selected for the filling height of the cylinder. In this work, 50% for filling height is used. The filled drum is then placed on a roller bench, which sets it in rotation at a constant speed. For this work, three different speeds of 44, 98, and 132 rpm are used. Depending on the speed and the investigated material, different characteristic motion profiles of the material appear after a short time, which are recorded with a camera and then evaluated by single image decomposition. It has become established that the flow regimes can be divided into the categories "slipping," "slumping," "rolling," "cascading," "cateracting," or "centrifuging" based on calculating the Froude number (Equation (20)).

$$Fr = \frac{\omega^2 R}{g} \quad (20)$$

The used rotation speeds give values for the Froude number of 0.06, 0.29, and 0.53, which put the experiments in the "cascading" and "cateracting" flow regime.

Depending on the flow behavior of the material, which can be between free-flowing and very cohesive, one or more characteristic angles are formed in the material during rotation. The rotating drum is one of the standard experiments in the investigation of powdery bulk materials and, along with the static angle of repose, is one of the most frequently performed DEM calibration experiments. The advantage of the experiment lies in the simple experimental setup and evaluation. The immediately possible comparison between the results of the DEM simulation and the experimental results allows a quick assessment of whether the simulation model is able to adequately represent the dynamic movement of real powders.

When looking at the dynamic angle of repose that occurs in the experiment some authors report, that an expansion of the particle bed is noticeable. Castellanos and colleagues^[10,23] report that this is due to air that gets entrained into the particle bed. To depict this effect in the DEM simulations the influence of the air on the particle movement has to be considered. The force relevant to the particle bed expansion is the drag force, which is not implemented by default in LIGGGHTS. The resistance force F_W for spherical particles was taken into account as an additional force via the formula 21 in the calculation equations of the force balance (Equation (1)). The drag coefficient ζ contained

therein was estimated for spherical spheres using the Formula (22) and is valid up to Reynolds numbers of 10^5 ,^[24] which for the application under consideration can never be achieved though. α_{CG} stands for a correction factor due to the coarse graining of the simulated particles. It has a value of 75–100 and is assumed to be constant for all simulations of the rotating drum.

$$F_w = \alpha_{CG} \zeta \rho_f \frac{\pi}{4} d_p^2 \frac{w_p^2}{2} \quad (21)$$

$$\zeta = \frac{1}{3} \left(\sqrt{\frac{72\nu_f}{w_p d_p}} + 1 \right)^2 \quad (22)$$

3. Experimental Work

The flow properties of pure NMC-622 in both new and aged conditions were investigated using a Schulze RST-01 ring shear cell. The NMC-622 (BASF) material was examined with one of the smallest available measuring cells, the XS type, to limit the use of material. Aging was induced by storing the NMC-622 in containers, which were not sealed from the ambient atmosphere for about 12 months. This was the material, which was referred to old NMC-622 in the subsequent discussion. New NMC-622 was referred to as NMC-622 material which was taken from a new batch and which was always stored sealed from ambient atmosphere. For the analysis in the ring shear cell, four different shearing stresses were calculated for each measuring point, which correspond to 20%, 40%, 60, and 80% of the nominal pre-shearing stress. The experiments were repeated at least three times. After a continuous series of measurements, the material was removed from the shear cell, loosened up and then added back to the measuring cell for a new series of tests.

The moisture content of the material was measured periodically during the ring shear cell experiments using a Kern DAB 100 moisture sensor. For the old NMC, the moisture content ranged from 0.23 to 0.49%_m with a mean of 0.37%_m. For the new NMC, the moisture content ranged from 0.12 to 0.25%_m with a mean value of 0.17%_m. The humidity of the old NMC-622 was thus slightly above the values for the new NMC-622. Overall, however, the moisture content of both materials could be regarded as fairly low.

3.1. Experimental Results

With Formula (23), the flowability of a powder could be calculated from the values of the consolidation stress σ_1 and the compressive strength σ_c (unconfined yield strength) of the material.^[25] The larger the value, the easier it was to bring the powder from the quiescent state to the flow state for a given value of compressive stress.^[25] It had become established to define ranges for the flowability value FFC to be able to compare the flow behavior of different powders.^[25] The classification of the powders examined according to their flowability provides a good point of reference when designing powder silos, for example, but would also be suitable for assessing how well dry battery powder could be processed for example in a calendar.

Table 1. Values for the flowability index FFC of new and old NMC-622 for different normal stress. Values in brackets give the simple standard deviation.

Normal stress	FFC old NMC-622	FFC new NMC-622
2 kPa	10.7 (±2.3)	11.1 (±4.8)
3 kPa	6.4 (±0.4)	6.5 (±1.8)
4 kPa	6.9 (±3.5)	6.5 (±2.7)
5 kPa	6.4 (±2.6)	6.8 (±1.9)

$$FFC = \frac{\sigma_1}{\sigma_c} \quad (23)$$

- 1) $FFC < 1$, not flowing;
- 2) $1 < FFC < 2$, very cohesive;
- 3) $2 < FFC < 3$, cohesive;
- 4) $4 < FFC < 10$, easy-flowing;
- 5) $10 < FFC$, free-flowing

Table 1 shows the determined flowability values for new and old NMC-622. It was found that the FFC values for both materials were flat in the range of normal stresses measured for both materials. The increase in the FFC value for a normal stress of 2 kPa was seen as an outlier in the measurements and was excluded from further considerations. This was also evident from the results for shear progressions over time, where high fluctuations of shear stresses were observed for a normal stress of 2 kPa which was considered an indication of poor measurability. Overall, the values for the flowability were 6 or higher and could therefore be categorized as “easy flowing” according to the classification.

Figure 4 shows the measured values for the static and dynamic friction coefficients in the Schulze Ring Shear Cell RST-01 for different normal stresses in the range from 2 to 150 kPa. Circles mark the values for aged NMC-622 and triangles mark the values for new NMC-622. For lower normal stresses up to 5 kPa, the error bars were fairly high. The reason for this lies in the accuracy of the ring shear cell tester for small normal stresses. Small deviations in the filling process in each run, lead to a larger error in the measured shear stresses while shearing the material. This makes a more accurate determination of

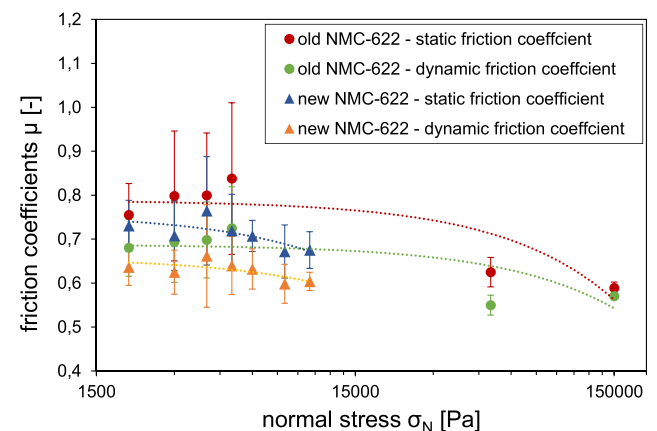


Figure 4. Experimental values for the static and dynamic friction coefficients for old and new NMC-622.

friction coefficients for lower normal stresses challenging. With higher normal stresses, the deviations get smaller. It is expected that small deviations when filling the ring shear cell have a smaller influence on the determination of the friction coefficients. However, smaller normal stresses were of interest, since the normal stresses in the rotating cylinder were fairly low (<3 kPa). The accuracy of the measurements for lower normal stress might be improved with a larger measurement cell with more volume. Despite this challenge, the measured values show a characteristic progression. Typically the friction coefficient gets lower for higher normal stresses. This was usually explained with two contributing factors to friction: adhesive and frictional forces. Since with higher normal stress, the adhesive contribution gets smaller compared to the frictional contribution, the overall resistance against flow decreases in relation to the normal stresses acting on the materials. Furthermore from the results, the static friction coefficients were always higher than the dynamic friction coefficients, which was to be expected. The old NMC-622 generated higher averaged values for both static and dynamic friction coefficients than the new NMC-622.

This might be explained by the fact that aged NMC-622, which had been in contact with the ambient air, undergoes chemical reactions that form an oxide layer on the surface which makes it overall rougher than was the case with new NMC, which had not yet any oxide layers formed on the surface. Therefore, in the measurements of the materials in the ring shear cell, aged NMC-622 showed slightly higher average static and dynamic coefficients of friction for all normal stresses. For a better analysis, scanning electron microscope (SEM) images of the new and old NMC-622 were taken. **Figure 5** shows the surfaces of individual NMC-622 particles. When examining the surface, elevations in the material for the aged NMC-622 were noticeable, which were not found in the new batch. Overall, the aged material appears rougher, the new one smoother, which also corresponds to the coefficients of friction measured in the ring shear cell. The roughness of the aged NMC-622 could be explained by the formation of oxide layers which lead to an enlargement of the edges. With the new material, these angular structures were not as pronounced. The SEM images could not be used to assess whether the oxide layers actually formed during the storage or aging of the NMC or whether they were manufacturing-related deviations.

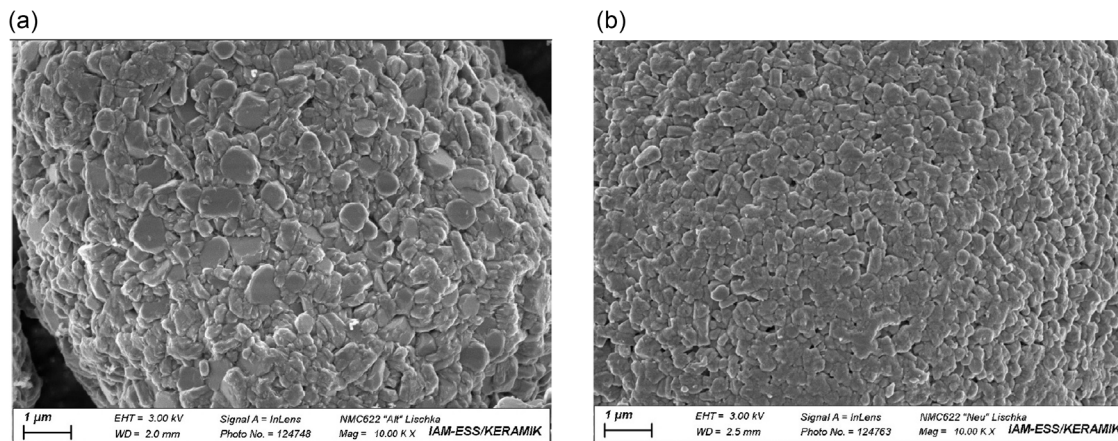


Figure 5. SEM images of the surface of a single NMC-622 particle for old and new NMC-622.

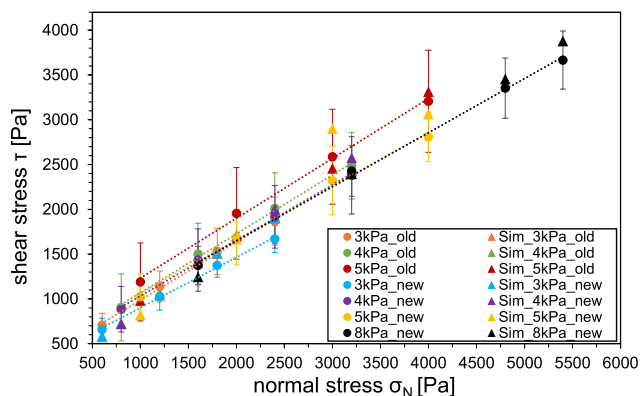


Figure 6. Comparison of experimental and simulated values for different normal stresses during shear-off in RST-01 ring shear cell. Error bars indicate the 95% confidence interval.

Further measurements would have to be made to clarify this. However, the different coefficients of friction measured in the ring shear cell could most likely be traced back to the different surface properties of the two materials.

3.2. Simulation Results for the Ring Shear Cell

Figure 6 shows the comparison of the point of incipient flow in the experiments and the simulated values for three different normal stresses 3, 4, and 5 kPa for old NMC-622 and four different normal stresses 3, 4, 5, and 8 kPa for new NMC-622. It could be seen that simulated values lie within the error range from the experiments and the agreement between simulation and experiment get generally better with higher normal stresses. Overall, the agreement for old NMC-622 was slightly better than for new NMC-622 which was also evident from the calculated values for the coefficient of determination R^2 , which was discussed further. Simulations for higher normal stresses for old NMC-622 had been performed but were omitted from this graph to enhance the visibility in the area of interest.

Table 2 and **3** show the values that were used for the simulation of the shearing of used NMC-622 material in the Schulze

Table 2. Overview of the used DEM parameters for the simulation of old NMC-622 with the Schulze RST-01 ring shear tester.

Normal stress [kPa]	Static friction coefficient particle–particle [-]	Dynamic friction coefficient particle–particle [-]	Static friction coefficient particle–wall [-]	Dynamic friction coefficient particle–wall [-]	Cohesion energy density particle–particle [J m^{-3}]	Cohesion energy density particle–wall [J m^{-3}]	Coefficient of restitution particle–particle [-]	Coefficient of restitution particle–wall [-]
3	0.582	0.566	0.05	0.01	231	30	0.5	0.5
4	0.591	0.577	0.05	0.01	362	30	0.5	0.5
5	0.642	0.632	0.1	0.05	482	30	0.5	0.5
50	0.625	0.55	0.1	0.05	1669	30	0.5	0.5
150	0.589	0.57	0.1	0.05	5100	30	0.5	0.5

Table 3. Overview of the used DEM parameters for the simulation of new NMC-622 with the Schulze RST-01 ring shear tester.

Normal stress [kPa]	Static friction coefficient particle–particle [-]	Dynamic friction coefficient particle–particle [-]	Static friction coefficient particle–wall [-]	Dynamic friction coefficient particle–wall [-]	Cohesion energy density particle–particle [J m^{-3}]	Cohesion energy density particle–wall [J m^{-3}]	Coefficient of restitution particle–particle [-]	Coefficient of restitution particle–wall [-]
3	0.591	0.577	0.05	0.025	244	30	0.5	0.5
4	0.642	0.632	0.05	0.025	335	30	0.5	0.5
5	0.625	0.55	0.05	0.025	378	30	0.5	0.5
6	0.589	0.57	0.05	0.025	388	30	0.5	0.5
8	0.589	0.57	0.05	0.025	425	30	0.5	0.5
10	0.589	0.57	0.1	0.05	594	30	0.5	0.5

RST-01 ring shear tester with the XS-type cell. The values for the static and dynamic friction coefficients as well as for the cohesion energy density for the particle–particle contacts were determined directly from the experiments and used in the simulations. Values for the static and dynamic friction coefficients as well as for the cohesion energy density for particle wall contacts were adjusted so that the agreement with experimental shear stresses was maximized. Cohesion energy density was expected to vary as well for particle–wall contacts; however, since the actual values could not be determined the value was set to a lower constant value of 30 J m^{-3} since it was expected that for smooth surfaces the cohesion energy between particles and wall were significantly below the cohesion energy densities between particle–particle contacts. It was possible to use a modified version of the Schulze ring shear tester that could measure the friction for particle wall contacts. The so-called wall friction ring shear tester was however not available for this work. Value variation was also done for the coefficient of restitution for particle–particle and particle–wall contacts since experimental values would require a sophisticated measuring device for single particle–particle and particle–wall contacts on the scale of few μm . To the best knowledge of the authors, such a device was not yet publicly available.

Table 4 gives the values for the coefficient of determination R^2 between all experiments and simulations in the ring shear cell for the different normal stresses. The R^2 was calculated from the difference for every data point of the experiment and the respective simulation data point, therefore giving a single value for the determination of the agreement of all data points. The R^2 values for old NMC-622 were in the range from 0.83 to 0.91, which indicated a good agreement between the experimental and the simulated values for the shear stresses. The values for new

Table 4. Values for the coefficient of determination R^2 between experiment and simulations.

Normal stress	R^2 old NMC-622	R^2 new NMC-622
3 kPa	0.90	0.60
4 kPa	0.83	0.60
5 kPa	0.85	0.69
8 kPa	–	0.77
10 kPa	–	0.70
50 kPa	0.91	–
150 kPa	0.85	–

NMC-622 were in the range from 0.6 to 0.77, which was slightly lower compared to the values of old NMC-622 but still indicate acceptable agreement between experiments and simulation.

Figure 7 shows the simulated progression of the shear stresses for three different normal stresses in the Schulze RST-01 ring shear tester for NMC-622. The black lines indicated the averaged shear stresses over time. The gray areas indicated the standard deviations for the repeated experiments. At least four experiments were done for each normal stress. The green lines indicated the simulated values of shear stresses. A shearing experiment consisted of the pre-shearing phase in which the nominal normal stress was applied. When the shear stress reached a stationary value during pre-shearing, a lower normal stress was applied for the first shear point. Typically the shear stress reached a local maximum and reaches a stationary value during shearing. Before the next normal shear point was applied the material was pre-sheared once again with the nominal normal force applied. One measurement usually consisted of

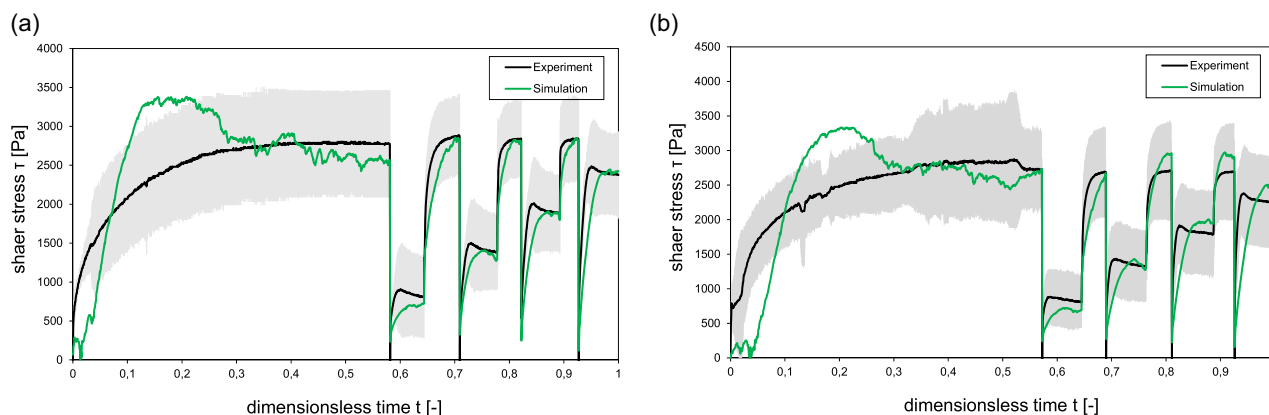


Figure 7. Comparison of experimental and simulated shear progressions over time in the Schulze RST-01 ring shear tester for a normal stress of 4 kPa. a) Results for old NMC-622 and b) for new NMC-622. Black lines indicate the averaged experimental values, gray areas indicate the 99.7% confidence interval and green lines indicate the simulation results.

four pre-shearing and four different shear points, although the number of shear points was arbitrary, four points were used to achieve a good compromise between accuracy and experimental burden for the calculation of the shear curves.

It could be seen from Figure 7 that the simulated progressions follow the experimental values in good agreement and fall in the area of the confidence interval (gray area). Agreement for the old NMC-622 material was slightly better than for new NMC-622 material, as was also seen from the coefficients of determination, reported earlier. It was suspected that the agreement for new NMC-622 could be improved by further investigation into the parameters for particle-wall friction, reducing the coarse-graining factor or adjustment of coefficient of restitution between particles and the walls. Since the agreement was acceptable, this was not done in the context of this work presented here.

From the simulation results of shear progressions also a typical overshooting in the pre-shearing phase was always observed. One possible explanation could be the effect of the coarse-grained particles. Since a lot less particles were simulated than there were in the real experiments, small pockets of simulated particles that block each other and create an interlocking effect might have an overall larger influence on the transmitted shear stresses to the lid of the shear cell. If this mechanical interlocking effect was resolved, the shear stress was only depended on the

frictional and adhesive forces, which then were reasonably well captured by the coarse-grained particles. Decreasing the coarse-graining factor could be checked to verify this hypothesis. Another possible explanation could be the varying rotational speed of the shear cell. Although it was said that rotating speed did not have influence on the results of the shear cell,^[25] the effect could only be studied if the experiments were done with a constant speed of the shear cell like it was done in the simulations.

3.3. Results for the Rotating Cylinder

Figure 8 gives the comparison of the dynamic angles at two different times of the experiment (1 and 3 s) in the rotating cylinders for a rotational speed of 44 rpm. The images (a and b) show the overlaid results for the experiment (light gray areas) and the simulation (black areas) without considering the drag force acting on particles. The images (c and d) show the overlay between the experiment and the simulation when the drag force was considered. It could be seen that at a rotational speed of 44 rpm the particles were moving fairly slow. Avalanching behaviour could be seen in the experiment where portions of the particle bed are breaking up. This periodical behavior could not be seen in the simulations. It is suspected that the coarse-graining factor

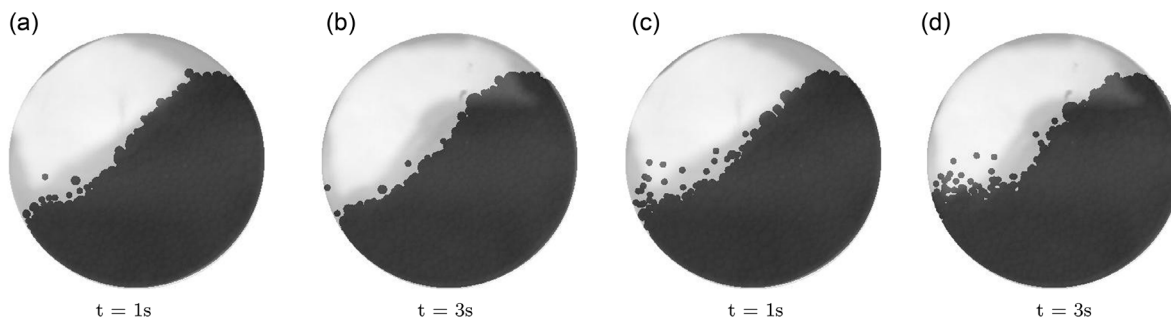


Figure 8. Comparison of experimental and simulated dynamic angle snapshots in a rotating cylinder for old NMC-622 with a rotation speed of 44 rpm. The pictures are an overlay of the experimental pictures (light gray) and the simulation results (black). The images a,b) show the comparison without enabled drag force in the simulations. The images c,d) show the comparison when the drag force is enabled in the simulation.

Table 5. Time-Averaged values of the average black pixel positions for x and y axis for experiment and simulations with and without drag force at a rotational speed of 44 rpm. Percentage values give the deviations between the experiment and simulation.

Average pixel position	Experiment	Simulation without drag force	Simulation with drag force
x -pos.	201.3	218.9 (+8.7%)	216.9 (+2.7%)
y -pos.	200.4	202.8 (+1.2%)	188.6 (+5.9%)

may be playing an influential role here. Avalanching was typically seen in cohesive powders and low rotational speeds. Comparing the simulation results with and without enabled drag force shows, that at low rotational speeds air entrainment was not a dominant effect in the particle bed. **Table 5** shows an improvement in the difference of the time-averaged pixel positions of the x -axis from 8.7% to 2.8% and a slight decrease in agreement from 1.2% to 5.9% for the average y -pixel position with enabled drag force. The overall agreement between the simulation results and the experiments at 44 rpm was considered acceptable although the avalanching phenomenon could not be seen in the simulations.

Figure 9 gives the comparison of the dynamic angles at two different times in the rotating cylinders for a rotational speed of 98 rpm. The images (a and b) show the overlaid results for the experiment and simulation without considering the drag force acting on particles. The images (c and d) show the overlay between particles and the simulation when the drag force was considered. It could be seen that at a rotational speed of 98 rpm the dynamic angle was different from the speed at 44 rpm. The particle bed was more expanded and was showing a typical “bend” type structure. It was suspected that because of the higher kinetic energy of the particles due to higher rotation speed, air was entrained with the particles which led to an expansion in the bed size. Comparing the simulation results with and without enabled drag force confirms, that considered the drag forces led to a better visual agreement between the simulation and experiment. **Table 6** shows also an improvement in the difference of the time-averaged pixel positions of the x and y axis from 10% to 6% and 8.1% to 2.4% with enabled drag force. With enabled drag force, there was still a small area in the middle-left area of the frames where the agreement could be improved. This

Table 6. Time-averaged values of the average black pixel positions for x and y axis for experiment and simulations with and without drag force at a rotational speed of 98 rpm. Percentage values given the deviations between the experiment and simulation.

Average pixel position	Experiment	Simulation without drag force	Simulation with drag force
x -pos.	197.1	216.6 (+10%)	208.9 (+6%)
y -pos.	184.3	199.2 (+8.1%)	179.8 (+2.4%)

might either be done by finding better DEM parameters or by lowering the coarse-graining factor. Overall, the agreement was still quite satisfactory.

Figure 10 gives the comparison of the dynamic angles for two different times in the rotating cylinder for a rotational speed of 132 rpm. The images (a and b) show again the overlaid results for the experiment and simulation without considering the drag force acting on particles. The images (c and d) show the overlay between particles and the simulation when the drag force was considered. It could be seen that at a rotational speed of 132 rpm the particle bed was expanded further due to entrained air. The expansion in the simulation was captured also when the drag force was enabled. **Table 7** shows an improvement in the difference of the time-averaged pixel positions of the x and y axis from 15% to 10% and 8.1% to 6.75% with enabled drag force. Overall, the agreement between the experiment and the simulation was again satisfactory even for high rotational speed.

For the highest rotational speed of 132 rpm, the deviations between experiment and simulation get more pronounced. It could be speculated that higher rotational velocities might introduce turbulence in the system, which could have an impact on bed expansion as well. If turbulence was introduced at higher speeds, the simplified approach of implementing the drag force model (as in this work) might not be enough to capture the effect. A CFD-DEM coupled approach might be needed to simulate the fluidization process more accurately.

4. Conclusion

Powdered NMC-622 cathode material was characterized using a Schulze ring shear cell and a rotating cylinder. The powder

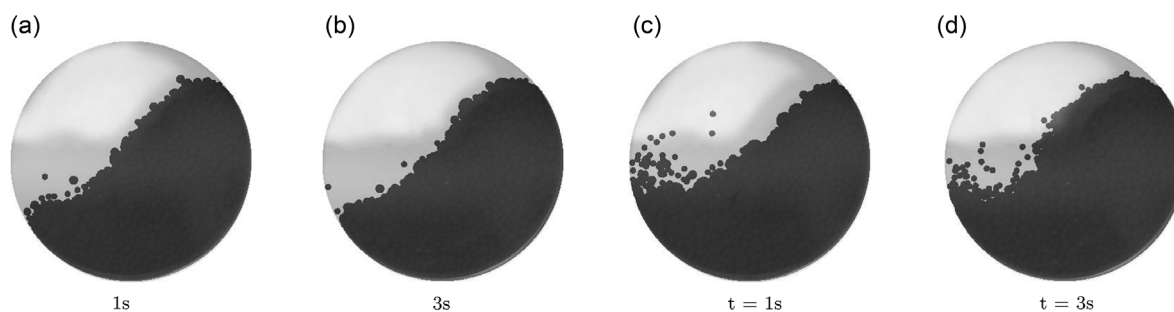


Figure 9. Comparison of experimental and simulated dynamic angle snapshots in a rotating drum for old NMC-622 with a rotation speed of 98 rpm. The pictures are an overlay of the experimental pictures (light gray) and the simulation results (black). The images a,b) show the comparison without enabled drag force in the simulations. The images c,d) show the comparison when the drag force is enabled in the simulation.

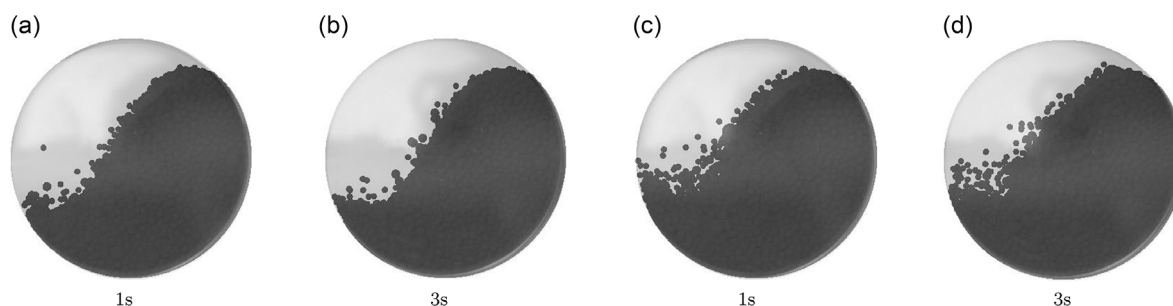


Figure 10. Comparison of experimental and simulated dynamic angle snapshots in a rotating drum for old NMC-622 with a rotation speed of 132 rpm. The pictures are an overlay of the experimental pictures (light gray) and the simulation results (black). The images a,b) show the comparison without enabled drag force in the simulations. The images c,d) show the comparison when the drag force is enabled in the simulation.

Table 7. Time-averaged values of the average black pixel positions for x and y axis for experiment and simulations with and without drag force at a rotational speed of 132 rpm. Percentage values give the deviations between experiment and simulation.

Average pixel position	Experiment	Simulation without drag force	Simulation with drag force
x -pos.	186.5	214.5 (+15%)	205.6 (+10%)
y -pos.	180.2	194.7 (+8.1%)	168.0 (+6.75%)

flowability of new and aged NMC-622 was determined for various normal stresses and the material was characterized as free-flowing ($FFC = 6$). Furthermore, the static and dynamic rolling friction coefficients were determined as a function of the normal stress for new and aged NMC-622 powder. The values were in a range from approx. 0.6 to 0.9. These parameters were used for a DEM simulation model to simulate the material behavior in the ring shear cell and a rotating cylinder using the coarse-graining approach. Both the characteristic shear curve and the dynamic flow behavior of the NMC-622 could be simulated with this model in good agreement with the experiments. It was found that for a more precise description of the dynamic angle of repose in the rotating cylinder, the air entrainment into the particle bed must be taken into account by considering the drag force acting on the particles. The proposed modeling is also suitable for a coarse-graining approach if a correction factor is taken into account. The material parameters of the NMC-622 obtained with the help of this calibration are suitable for carrying out further simulations of processes relevant to the production of Li-ion batteries, such as the dry mixing process with conductive additives like carbon black. This is planned in future work.

Acknowledgements

The authors gratefully thank the Federal Ministry of Education and Research for funding this work in the project Sim4Pro (grant number 03XP0242B) within the ProZell Cluster.

Open Access funding enabled and organized by Projekt DEAL.

Conflict of Interest

The authors declare no conflict of interest.

Data Availability Statement

The data that support the findings of this study are available from the corresponding author upon reasonable request.

Keywords

calibration, discrete element method (DEM), Li-ion battery cells, NMC-622, rotating cylinder, Schulze RST-01 ring shear cell, simulations

Received: July 28, 2022

Revised: October 17, 2022

Published online:

- [1] D. Schreiner, J. Lindenblatt, F. J. Günter, G. Reinhart, *Procedia CIRP* **2021**, *104*, 91.
- [2] R. Ge, D. J. Cumming, R. M. Smith, *Powder Technol.* **2022**, *403*, 117366.
- [3] A. C. Ngandjong, T. Lombardo, E. N. Primo, M. Chouchane, A. Shodiev, O. Arcelus, A. A. Franco, *J. Power Sources* **2021**, *485*, 229320.
- [4] C. S. Gimenez, C. Schilde, L. Froböse, S. Ivanov, A. Kwade, *Energy Technol.* **2019**, *8*, 1900180.
- [5] C. Sangrós Giménez, B. Finke, C. Nowak, C. Schilde, A. Kwade, *Adv. Powder Technol.* **2018**, *29*, 2312.
- [6] J. K. Mayer, L. Almar, E. Asylbekov, W. Haselrieder, A. Kwade, A. Weber, H. Nirschl, *Energy Technol.* **2020**, *8*, 1900161.
- [7] E. Asylbekov, R. Trunk, M. J. Krause, H. Nirschl, *Energy Technol.* **2021**, *9*, 2000850.
- [8] LIGGGHTS Hertz particle contact model, https://www.cfdem.com/media/DEM/docu/gran_model_hertz.html (accessed: July 2022).
- [9] LIGGGHTS EPSD rolling friction model, https://www.cfdem.com/media/DEM/docu/gran_rolling_friction_epsd.html, (accessed: July 2022).
- [10] A. Castellanos, J. M. Valverde, A. T. Pérez, A. Ramos, P. K. Watson, *Phys. Rev. Lett.* **1999**, *82*, 1156.
- [11] D. S. Nasato, C. Goniva, S. Pirker, C. Kloss, *Procedia Eng.* **2015**, *102*, 1484.
- [12] H. Nakamura, H. Takimoto, N. Kishida, S. Ohsaki, S. Watano, *Chem. Eng. J. Adv.* **2020**, *4*, 100050.
- [13] C. Bierwisch, T. Kraft, H. Riedel, M. Moseler, *J. Mech. Phys. Solids* **2009**, *57*, 10.
- [14] Y. T. Feng, D. R. J. Owen, *Comput. Part. Mech.* **2014**, *1*, 159.
- [15] J. Hlosta, L. Jezerská, J. Rozbroj, D. Žurovec, J. Nečas, J. Zegzulka, *Processes* **2020**, *8*, 222.

- [16] X. Cao, Z. Li, H. Li, X. Wang, X. Ma, *Processes* **2021**, *9*, 605.
- [17] J. Pachón-Morales, P. Perré, J. Casalinho, H. Do, D. Schott, F. Puel, J. Colin, *Adv. Powder Technol.* **2020**, *31*, 1500.
- [18] L. Legoux, C. Gatamel, M. Milhe, H. Berthiaux, *Powder Technol.* **2017**, *305*, 609.
- [19] J. Pachón-Morales, H. Do, J. Colin, F. Puel, P. Perré, D. Schott, *Adv. Powder Technol.* **2019**, *30*, 732.
- [20] T. A. H. Simons, R. Weiler, S. Strege, S. Bensmann, M. Schilling, A. Kwade, *Procedia Eng.* **2015**, *102*, 741.
- [21] O. Baran, A. DeGennaro, E. Ramé, A. Wilkinson, *AIP Conf. Proc.* **2009**, *1145*, 409.
- [22] J. Yang, P. Bunchatheeravate, S. C. Thakur, J. W. Bullard, J. S. Curtis, *AIChE J.* **2021**, *67*, e17090.
- [23] A. Castellanos, J. M. Valverde, M. A. S. Quintanilla, *Phys. Rev. E* **2002**, *65*, 061301.
- [24] M. Kraume, *Transportvorgänge In Der Verfahrenstechnik - Grundlagen Und Apparative Umsetzung*, 2nd ed., Springer, Berlin **2012**.
- [25] D. Schulze, *Powders And Bulk Solids - Behavior, Characterization, Storage And Flow*. 2nd ed., Springer, Berlin **2008**.